Post-Print

This is the accepted version of:

The final publication is available at https://doi.org/10.1017/aer.2023.112

Access to the published version may require subscription.

Permanent link to this version
http://hdl.handle.net/11311/1257164

Wind Tunnel Test of Full-Scale Wing-Propeller System of a eVTOL Aircraft

L. Riccobene
D. Grassi

Politecnico di Milano
Dipartimento di Scienze e Tecnologie Aerospaziali
Milan
Italy

J. N. Braukmann

German Aerospace Center (DLR)
Institute for Aerodynamics and Flow Technology
Göttingen
Germany

M. Kerho and G. Droandi

Archer Aviation
Palo Alto, CA
USA

A. Zanotti [*]
alex.zanotti@polimi.it

Politecnico di Milano
Dipartimento di Scienze e Tecnologie Aerospaziali
Milan
Italy

[*] **Corresponding author**

ABSTRACT

The present paper describes the results of an experimental wind tunnel test campaign aimed at investigating the aerodynamic performance and flow physics related to a wing section equipped with two propellers mounted on a boom. The configuration investigated is meant to be representative of a full-scale eVTOL aircraft in cruise flight condition. The use of full-scale components of an eVTOL aircraft made this setup a quite advanced experiment in the recent literature. Pressure measurements and an Infrared Thermography technique were used during the test campaign, respectively to evaluate localized effects induced by the propeller blowing on the wing and to provide a quantitative evaluation of the amount of laminar flow on the wing surface with and without the influence of the propeller at different thrust conditions.

NOMENCLATURE

BL	Boundary Layer
AD	Actuator disk
AL	Actuator line
VPM	Vortex Particle Method
CFD	Computational Fluid Dynamics
C_p	Pressure coefficient
eVTOL	Electric Vertical Take–off and Landing
FoV	Field of View
GVPM	Large Wind Tunnel Politecnico di Milano
IRT	Infrared Thermography
PIV	Particle Image Velocimetry
rpm	revolutions per minute
UAM	Urban Air Mobility
LWIR	Longwave Infrared
U_∞	Wind tunnel freestream velocity
x	Chord-wise direction
y	Span-wise direction
C_l	Sectional lift coefficient
$\overline{C}_{l,np}$	Reference sectional lift coefficient (w/o propeller)

Greek Symbol

α	Angle of attack (degrees)
Ω	Rotational frequency (rpm)

1.0 INTRODUCTION

The emerging concept of Urban Air Mobility (UAM) envisions a safe, efficient, sustainable, and affordable air transportation system that will expand existing ground transportation networks to short-range flights and will use innovative electric vertical takeoff and landing (eVTOL) vehicles to transport passengers and deliver goods within overcrowded metropolitan areas[1]. In recent years, major aviation and automotive manufacturers, an increasing number of new start-ups, as well as research institutions and universities around the world have devoted

considerable effort to maturing key technologies supporting vertical lift. These include distributed electric propulsion systems, new battery architectures and technologies, autonomous systems, and new vehicle concepts which incorporate these emerging technologies. The different architectures of these new concepts are diverse. Recent literature[2,3] compiles the most promising configurations for UAM purposes. The common feature clearly distinguished is related to the use of multiple propellers, typically mounted on a single or dual lifting surface. Consequently, critical aspects to be investigated are the complicated flow patterns related to the aerodynamic interaction between the wing and the propellers as well as the effects of such interactions on propeller loads.

Significant efforts have been spent in recent years to investigate both the propeller–propeller[4] as well as the wing–propeller aerodynamic interaction with application to eVTOL and tiltrotor configurations. In particular, wind tunnel campaigns involving several measurement techniques such as Particle Image Velocimetry (PIV), surface visualizations and total pressure wake surveys have been performed to gain insight into the interactional flow features characterising wing mounted propeller configurations[5]. Great effort was provided in this research field by TU Delft. An experimental study on this topic was conducted by Sinnige et al.[6] aimed to address the lack of comprehensive analyses of the aerodynamic interaction effects by providing a detailed aerodynamic analysis of the wingtip-mounted configuration. The study involved integral and local force measurements and comprehensive flow field evaluations through an experimental approach. Nevertheless, these experimental studies are performed over scaled wing-propeller models, thus not allowing a complete representation of flow behaviour around a full-scale eVTOL aircraft prototype.

Experimental databases available in literature for wing-propeller interactional studies represent an essential tool for the validation of Computational Fluid Dynamics (CFD) solvers with different levels of fidelity, as shown by the works by Alvarez et al.[7] and Zhou et al.[8] that used respectively a mid-fidelity and a high-fidelity numerical approach for the simulations of wing-propeller systems. Recently, Stokkermans et al.[9] explored the use of RANS solvers for simulating wingtip-mounted propellers with the goal of reducing computational costs while accurately capturing propeller-wing interactions. To address this issue, the authors evaluated the accuracy of RANS simulations for this particular configuration and explored the use of actuator-disk (AD) and actuator-line (AL) models. Last year, Van Arnhem in his doctoral dissertation exploited the effects of a wing tip mounted propeller mounted on a tailplane but also on the complete aircraft. Van Arnhem, in his doctoral dissertation[10], studied unconventional propeller integration on airframe including propellers that are mounted to the horizontal tailplane.

Recent advances in the use of Infrared Thermography (IRT) for boundary layer (BL) transition measurements[11] is an additional experimental tool to enhance knowledge about the flow patterns around these novel aircraft configurations. IRT has been effectively used to evaluate the transition point of laminar-to-turbulent flow within a wing BL[12] and has also been successfully used on helicopter propellers[13].

The current paper describes the results of an experimental investigation performed in the framework of a collaboration between Politecnico di Milano, German Aerospace Center (DLR) and Archer Aviation. In particular, wind tunnel tests were performed in the Politecnico di Milano wind tunnel[14]. The goals of the campaign were:

- To investigate and characterize wing-boom-propeller interactions in cruise and near-cruise conditions for a eVTOL type configuration.

- To verify and calibrate aerodynamics prediction tools used for vehicle design and performance evaluation such as high-fidelity CFD tools like NASA's Overflow[15] and Fun3D[16] solvers and as well as mid-fidelity tools like DUST, a panel code coupled with a state-of-the-art wake solver based on vortex particle method (VPM)[17].

- To evaluate the effects of the propeller slipstream on the wing BL to gain deeper insights on interactional effects typical of eVTOL aircraft configuration.

The novel aspect of the test setup with respect to similar experimental works in recent literature was the use of full-scale components of Archer's Maker eVTOL aircraft, see Fig. 1. The experimental setup was based on the use of full-scale Maker's aircraft tilter (powered) and lifter (stowed, unpowered) propeller units, full-scale Makers's boom and a full-scale wing representative of Maker's wing and built using the same airfoil section. Archer's Maker aircraft is a full-scale demonstrator that helped to inform the design and build of Archer's production aircraft - Midnight. Archer's Maker aircraft was used to validate Archer's 12-tilt-6 configuration. Flight test results were consistent with Archer's expectations, providing important validation for systems, instruments, and acoustics. Moreover, data and learning gathered on the way to achieving full wing-borne transition flight was used to inform Midnight's development. Indeed, Maker's successful completion of its flight test program demonstrates the technology required to fly UAM missions with eVTOL aircraft exists today and is ready for commercialization.

Figure 1. Picture of the Archer Maker's aircraft.

The experimental test setup, aimed to acquire data on a representative full-scale eVTOL aircraft in cruise flight conditions, represents a quite advanced experiment with respect to the ones described in recent literature. Indeed, different measurement techniques were employed, including pressure measurements on the wing surface and IRT. In particular, the use of pressure measurements enabled investigation of the effect of propeller blowing on local wing aerodynamic performance. On the other hand, the use of IRT enabled the investigation of propeller-wing aerodynamic interactions affecting BL transition on the wing as well as the effects on BL transition due to wing angle of attack, propeller rotational speed, propeller collective, and nacelle tilt angle. The present paper describes a selection of the comprehensive data base collected by wind tunnel test measurements. For the sake of confidentiality, results

are presented without numbers on graph axes. Nevertheless, this choice does not alter the readers' comprehension of the physical phenomena investigated in the present test activity.

The paper is organized as follows. Section §2 provides the description of the experimental setup used for the test, including a description of the measurement techniques employed. Section §3 presents the discussion of static pressure measurements and IRT results. Finally, conclusions are drawn in Section §4.
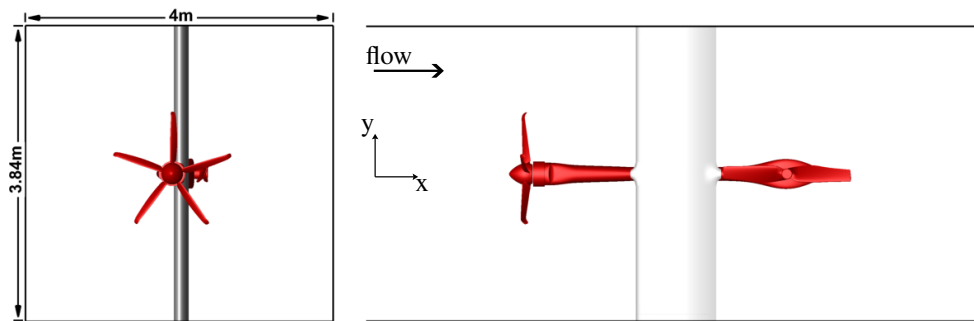
2.0 EXPERIMENTAL SETUP

Figure 2. Wind tunnel setup showing relative model/tunnel dimensions. Left) side view, Right) top view.

A comprehensive wind tunnel test campaign was performed in the $4\,\mathrm{m} \times 4\,\mathrm{m}$ low turbulence test section of the GVPM facility of Politecnico di Milano[14]. The GVPM has a maximum speed of $55\,\frac{\mathrm{m}}{\mathrm{s}}$ and a turbulence level less than $0.1\,\%$. A representative untwisted, untapered, straight full-scale wing section model was purposely manufactured for this test. Maker's wing airfoil section was used to loft the wing model. The model was mounted vertically in the tunnel, spanning the test section from floor to ceiling. The model was installed on the test section turn table that was used to precisely set the angle of attack. A full-scale model of Maker's forward tilter and aft lifter propellers were mounted on the wing model via an under-slung boom which extended upstream and downstream of the wing. During the experimental campaign the tilter propeller was powered (rotating), while the aft-mounted lifter propeller was fixed in the cruise position and aligned with the free-stream. The model/propeller setup in the tunnel was sized to minimize wall interference. Relative model/tunnel dimensions are shown in Fig.2. Typical corrections to advance ratio were 1.0-1.3%. The wind tunnel setup is shown in Fig.3.

2.1 Pressure measurements setup

The wing and boom surfaces were equipped with a total of 256 surface static pressure taps distributed as shown in Figure 4. The pressure taps on the wing surface were positioned in four belts equipped with 40 taps each. Pressure measurements were performed using eight low-range 32-port ESP-32HD pressure scanners embedded inside the wing model, acquired
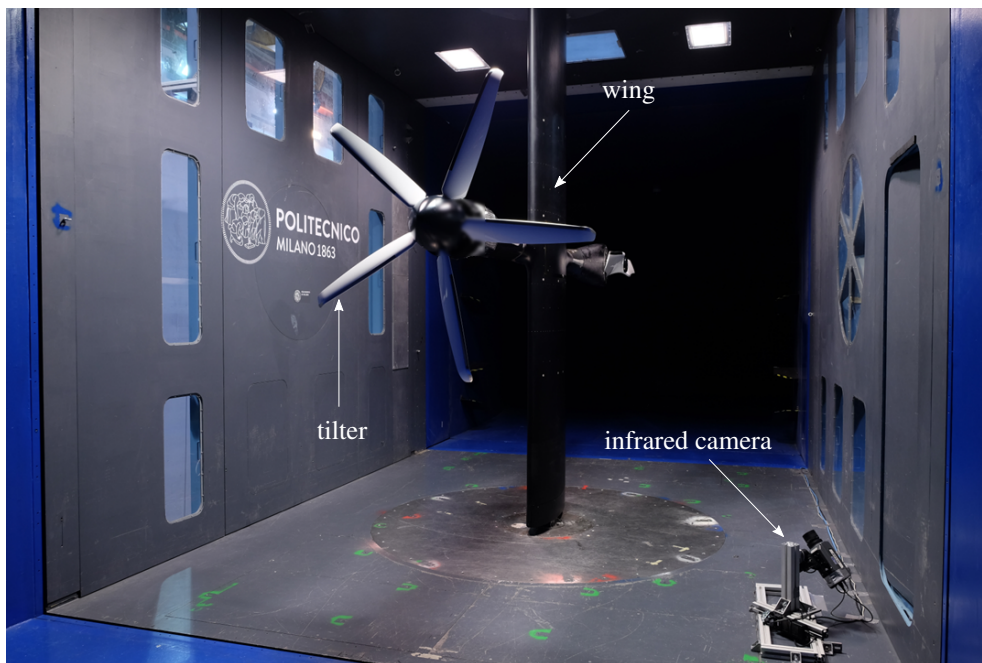
Figure 3. Maker's full-scale wing section model with propellers mounted in the GVPM test section. For thermography runs, the IR camera can be seen in the bottom right corner.

using DTC-Initium pressure scanning system. Acquisition time was 10 seconds for each test individual test point.

2.2 Infrared Thermography measurements setup

The baseline wing airfoil section was designed to achieve a certain amount of laminar flow. A main benefit of laminar flow is reduced drag, which translates into reduced power requirements and/or increased range. Due to the complex interaction between the periodic blade wake and the wing airfoil, with different regions of upwash and downwash, it's extremely difficult to reliably predict the actual amount of achievable laminar flow. During the present wind tunnel test IRT was used to evaluate quantitatively the amount of laminar flow for the baseline airfoil section and also for the wing airfoil under the influence of the propeller at different thrust conditions. The IRT instrumentation consisted of a FLIR A6751 LWIR Camera equipped with a Strained-Layer Superlattice sensor with 640×512 px resolution (square pixel size of $15\,\mu m$ edge). The thermal sensitivity of the sensor is below $45\,mK$. The camera was robustly attached to the wind tunnel floor by means of a metallic support structure (see Fig.2). A set of markers made of silver conductive paint dots were applied to the upper surface of the wing model in order to have known locations on the curved surface useful to map the images on the actual wing geometry. The markers were smoothed to avoid any roughness that could accelerate or trigger premature transition. Due to its size and the possible interference with other sensors, the model isn't equipped with an internal heating system, thus the test procedure was to heat up the tunnel free-stream air with the heat exchanger disabled, resulting in the model being cooler than the air. A small temperature difference of $2\,°C$ to $3\,°C$ between
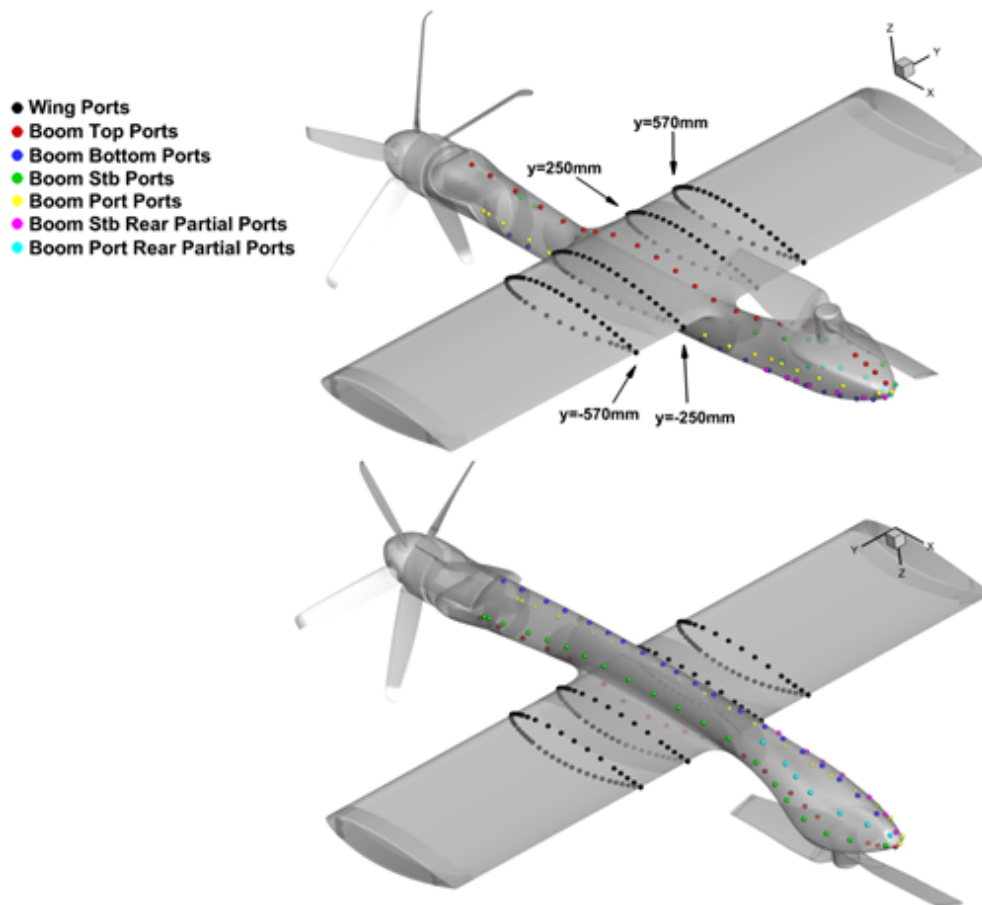
Figure 4. Scheme of pressure measurements setup.

the model and free-stream flow is sufficient to capture the differences in heat exchange between the laminar and turbulent BLs. Two different fields of view over the wing upper surface, above and below the boom, were considered for the IRT measurements. The measurements included conditions with different wing angles of attack, tilter propeller rotational speeds, blade collective angles, and nacelle angles, as well as wind tunnel free stream velocities. For each model test condition and field of view a series of 500 individual images were acquired with an acquisition frequency of 100 Hz and an exposure time (integration time) of 131.5 μs.

3.0 RESULTS AND DISCUSSION

3.1 Pressure Measurements

This section presents a selection of pressure measurements obtained during the test campaign. Pressure measurements included a wide set of test conditions used to evaluate the effect of the tilter propeller interaction with the wing performance in cruise flight condition. For all test conditions the lifter propeller was kept stowed. Test points included different sweeps of wing

angle of attack, tunnel speed, propeller tilt angle, blade collective angle, and propeller rotational speed. In the following, test results obtained for a representative cruise flight condition, i.e. with zero deflection of tilter propeller shaft angle and $U_\infty = 50\,\frac{m}{s}$, are presented and discussed.

Figure 5 shows the pressure coefficient distributions measured on the four wing belts at a constant propeller rotational speed of $1000\,\mathrm{rpm}$ and at wing angles of attack ranging from $-2.5°$ to $5°$.
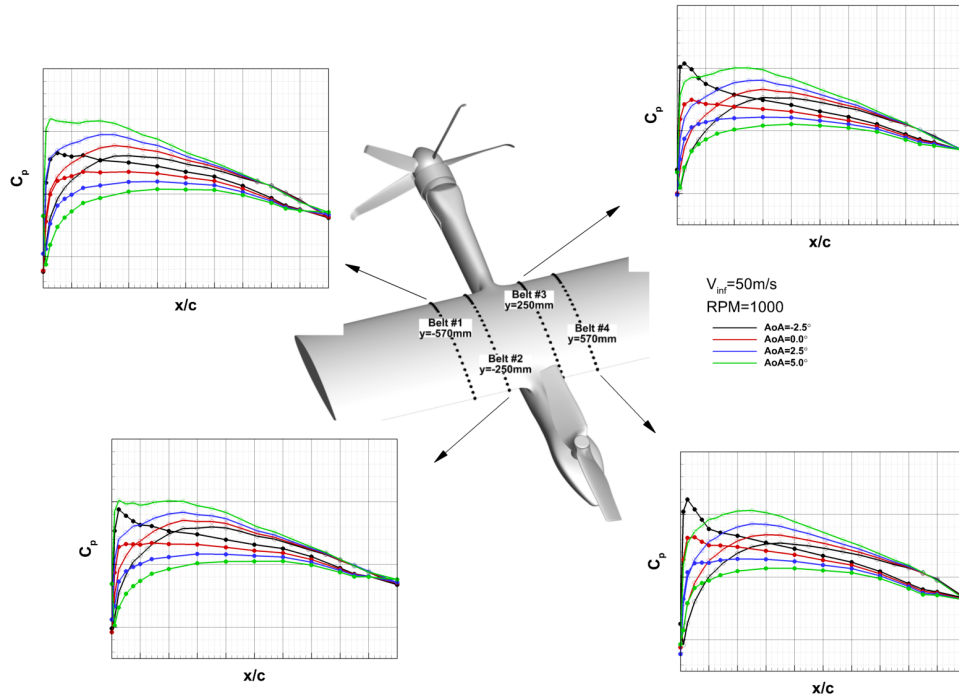

Figure 5. Static pressure measurements results over the wing with powered tilter propeller ($1000\,\mathrm{rpm}$) at different angles of attack, $U_\infty = 50\,\frac{m}{s}$.

The pressure distribution on the wing changes along the span of the model as a result of the induced effect of the propeller slipstream on the wing as well as the propeller sense of rotation. This is clearly visible from the comparison of the chord-wise pressure coefficient distributions measured over the four instrumented wing sections for a given angle of attack. For instance, the propeller induces a local upwash that has the effect of increasing the local angle of attack on belts #1 and #2. On the other hand, belts #3 and #4, located on the other side of the boom, are subject to a downwash that decreases the local angle of attack. The effect is further magnified by comparing results over the outer belts #1 and #4, where the vertical velocity component induced by the propeller is higher compared to the inboard belts.

Also discernable in the pressure distributions is the effect of angle of attack on the airfoil upper surface favorable pressure gradient. The magnitude and extent of the favorable pressure gradient has a direct effect on the BL transition location. As expected, as the angle of attack of the model increases, the favorable pressure gradient near the leading-edge of the wing suction

side (i.e. the upper surface of the wing) decreases becoming less favorable. As this favorable gradient decreases, one would expect the BL transition location to move forward towards the leading edge. The BL transition location depends primarily on the characteristics of the wing airfoil section and it is driven by the angle of attack of the wing. Other factors may also influence the transition location including the propeller interaction effects and tunnel flow quality.

The pressure measurements on the four wing belts shown in Figure 5 have been integrated to obtain the corresponding sectional lift coefficients C_l in order to quantify the effect of the tilter propeller slipstream on the wing. The results are scaled with respect to a reference sectional lift coefficient $\bar{C}_{l,np}$ obtained by averaging the local lift coefficients on the four belts measured with the propeller turned off at fixed wing angle of attack ($\alpha = 2.5°$) and at a given wind tunnel freestream velocity ($U_\infty = 50\,\frac{m}{s}$). The ratio between the sectional lift coefficient C_l and the reference lift coefficient $\bar{C}_{l,np}$ is shown in Fig. 6 as function of angle of attack at fixed rotational speed of the propeller for each belt.
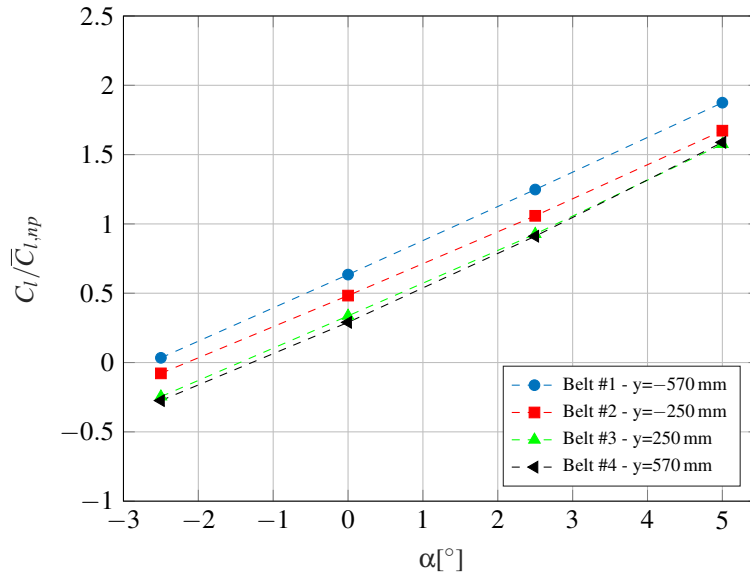

Figure 6. Ratio between sectional lift coefficient C_l and the reference sectional lift coefficient $\overline{C}_{l,np}$ over the wing with powered tilter propeller (1000 rpm) as function of angle of attack at different spanwise positions, $U_\infty = 50\,\frac{m}{s}$.

From Fig. 6, the upwash induced by the propeller on the left side of wing and experienced by the sections corresponding to belts #1 and #2 has the effect to increase the lift on this portion of the wing with respect to the opposite side where the propeller rotation induces a local downwash (belts #3 and #4). The lift variation between belts #1 and #2 in the upwash region of the wing is higher than the one observed between belts #3 and #4. Furthermore, sectional lift coefficients evaluated on belts #3 and #4 are fairly similar throughout the whole range of angles of attack tested. Since the wing is straight wing, changes in the pressure distribution and local lift coefficient are due to the 2D airfoil contour and angle of attack. Any spanwise differences in the distribution and lift coefficient are attributable to the propeller and its sense of rotation, which induces upwash/downwash velocities on the sections of the wing model depending on their position relative to the propeller axis.
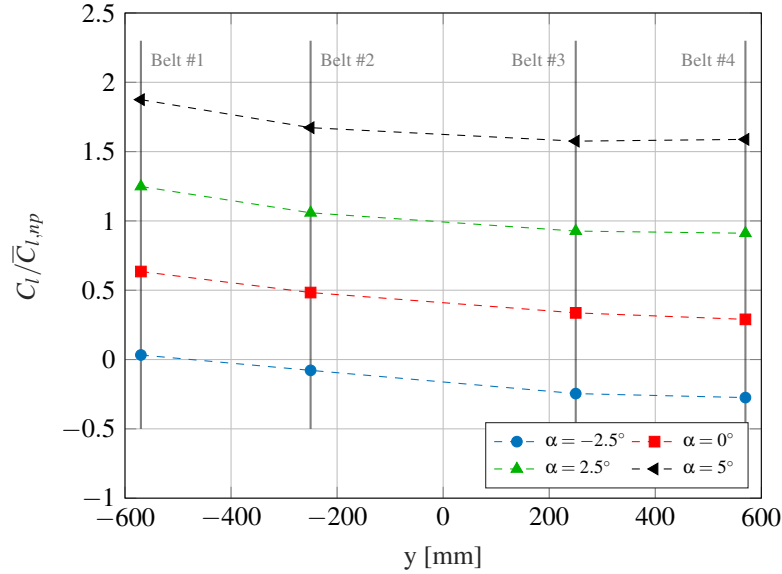
Figure 7. Ratio between sectional lift coefficient C_l and the reference sectional lift coefficient $\overline{C}_{l,np}$ over the wing with powered tilter propeller ($1000\,\text{rpm}$) as function of spanwise coordinate at different angles of attack, $U_\infty = 50\,\frac{\text{m}}{\text{s}}$.

The non-uniform lift distribution promoted over the wing span by the propeller slipstream is clearly highlighted in Fig. 7, where the ratio of sectional lift coefficients $C_l/\overline{C}_{l,np}$ is shown as function of the belt spanwise position at a fixed propeller rotational speed and for different angles of attack. Figure 7 shows that the wing sectional lift coefficient monotonically decreases going from belt #1 to belt #4. This behavior is fairly consistent for all the angles of attack analyzed. A net decrease of sectional lift coefficient occurs in the upwash region of the wing between belt #1 and #2 while in the downwash region between belt #3 and #4 the sectional lift coefficient reaches a plateau, particularly at higher angles of attack.

Figure 8 shows a comparison between the pressure distributions measured on the four belts of the wing with both the propeller spinning at different rotational speeds and turned off, at fixed wing angle of attack ($\alpha = 2.5°$) and at a given wind tunnel freestream velocity ($U_\infty = 50\,\frac{\text{m}}{\text{s}}$). The powered test cases are presented with the tilter propeller operating at a rotational speed ranging from $700\,\text{rpm}$ to $1100\,\text{rpm}$ to better illustrate the propeller rotational speed effects on the pressure distributions.

The pressure distributions measured on the wing belts show similar trends at high propeller rotational speed settings ($1000\,\text{rpm}$ and $1100\,\text{rpm}$). The effect of the propeller slipstream on the pressure distributions is noticeable on the outer belts (#1 and #4) when the powered cases are compared to the unpowered one. The effect of the propeller slipstream decreases on the inner belts (#2 and #3) where the differences with respect to the unpowered case are fairly small. At low propeller rotational speed setting ($700\,\text{rpm}$) the effects induced by the propeller slipstream on the wing model changes considerably with respect to the high rotational speed cases. The combination of propeller rotational speed and wind tunnel freestream velocity ($U_\infty = 50\,\frac{\text{m}}{\text{s}}$) produces an inflow that drives the propeller in windmill state. The pressure distributions measured on the wing in this condition show an opposite trend when compared to the high rotational speed cases and are qualitatively similar to the pressure distributions
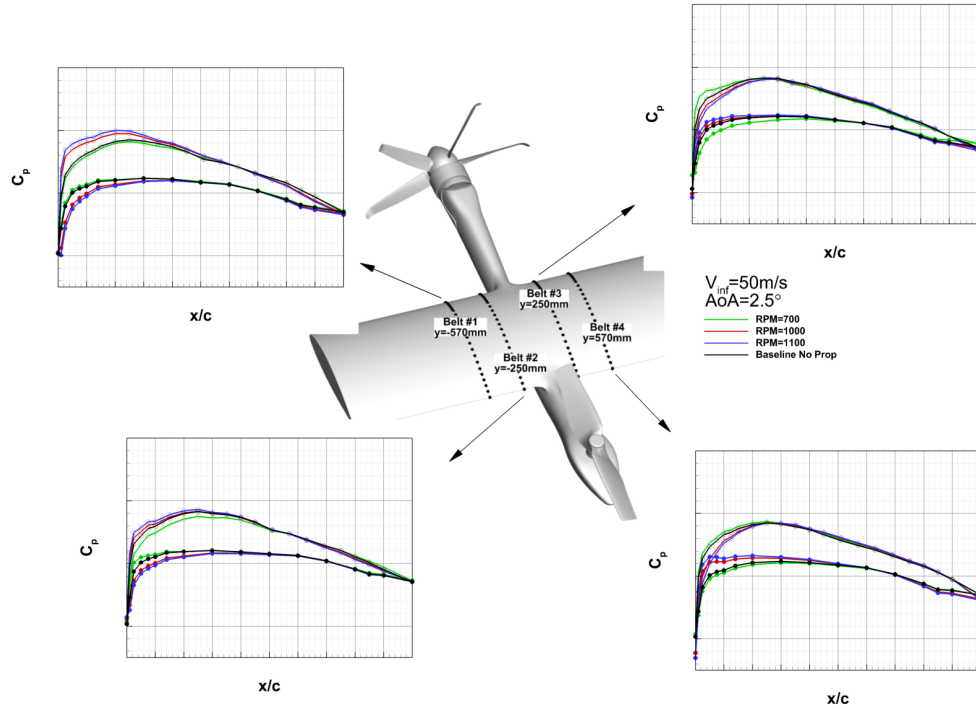
Figure 8. Static pressure measurements results over the wing with and without powered tilter propeller (700 rpm to 1100 rpm) at $\alpha = 2.5°$, $U_\infty = 50\,\frac{m}{s}$.

measured with the propeller turned off.

The effects produced by the propeller slipstream on the wing are clearly illustrated in Fig. 9 where the ratio of sectional lift coefficients $C_l/\overline{C}_{l,np}$ on each belt is shown as function of their spanwise coordinate with both the propeller spinning and turned off. Sectional lift coefficients $C_l/\overline{C}_{l,np}$ are compared at a fixed angle of attack ($\alpha = 2.5°$) and considering the same range of propeller velocities between 700 rpm and 1100 rpm. Figure 9 confirms that the flow around the wing is highly influenced by the propeller slipstream which provides a local opposite sectional lift variation with respect to its rotational axis. On the other hand, when the propeller is turned off, the lift distribution across the wing span shows a fairly flat behaviour as expected. This proves that propeller rotational speed and its sense of rotation are directly responsible for the asymmetry in the local flow around the portion of the wing blown by the propeller wake. The absolute value of the sectional lift coefficient variation provided at propeller rotational speeds equal to 1000 rpm and 1100 rpm is quite higher in the upwash region (belts #1 and #2), as previously observed. The effect on local wing airloads is more apparent at 1100 rpm. At 700 rpm the propeller is in windmill state and an opposite variation of local sectional lift with respect to propeller rotation axis can be observed.
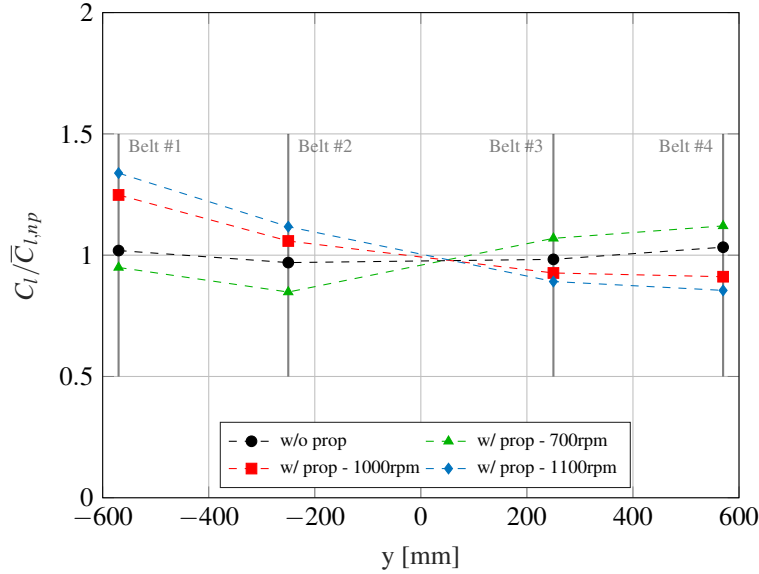
Figure 9. Ratio between sectional lift coefficient C_l and the reference sectional lift coefficient $\overline{C}_{l,np}$ over the wing as function of spanwise coordinate with and without powered tilter propeller at $\alpha = 2.5°$, $U_\infty = 50\,\frac{m}{s}$.

3.2 Infrared Thermography Measurements

The images displayed in Fig. 10 illustrate the surface temperature distribution on the suction side of the wing as a function of angle of attack. The images were obtained from the IRT survey carried out on the wing model with the tilter propeller removed from the boom and at fixed wind tunnel freestream velocity ($U_\infty = 40\,\frac{m}{s}$). The figure shows the average intensity distributions over the wing model at different angles of attack α ranging from $\alpha = -2.5°$ (leftmost image) to $\alpha = 10°$ (rightmost image). The x- and y-axes represent the chord and span of the wing respectively, whereas the surface temperature is given as a gray scale distribution averaged over the 500 individual recordings. The images were mapped onto a 3D grid of the wing's surface using the in house DLR software ToPas[18].

Figure 10 shows that the temperature at the leading-edge of the wing is less than that at the trailing-edge (darker gray scale level). This temperature difference is the effect of the flow behaviour on the wing's surface. For a laminar region, turbulent mixing is reduced and thus the heating of the wing's surface is reduced, while in a turbulent region the heat exchange is increased and thus the wing is heated more effectively. This effect can be exploited to measure the position of BL transition with IRT. Within the global measured field-of-view (FoV) depicted in Fig. 10 the temperature distribution is symmetric with respect to the y-axis, which is expected based on the straight wing symmetric geometry (above and below the boom). The images displayed in Fig. 10 show that the transition location moves towards the leading edge as the angle of attack of the wing increases, as expected. The influence of the boom can be seen in the region around the y-axis ($y/c = -0.1...0.1$), but since the map temperature is almost constant, no valuable information can be inferred in this portion of the wing. Instead the influence of pressure taps on the wing's surface as spanwise "wedges" can be observed as narrow areas of local forward movement of the transition position (see the case
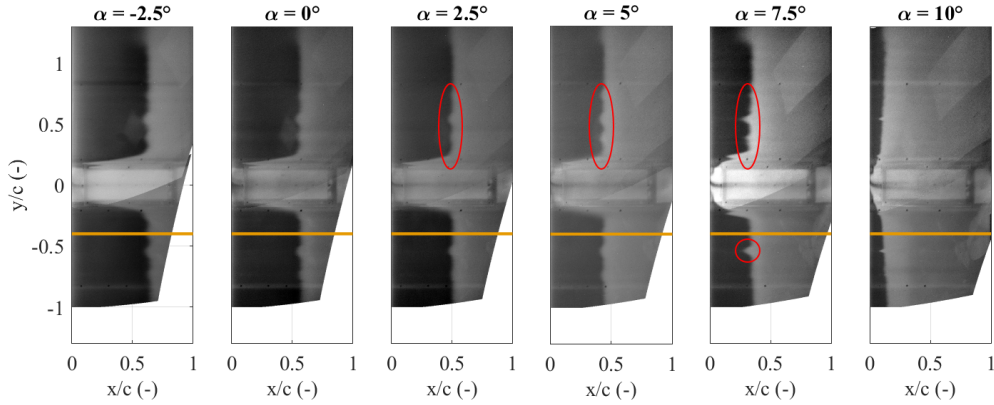
Figure 10. Average intensity distributions at different pitch angles α and an inflow velocity of $U_\infty = 40$ m/s without the propeller mounted. Minor disturbances in the shape of the transition line due to the presence of surface static pressure taps ("wedges") are highlighted in red.

$\alpha = 7.5°$ at spanwise positions $y/c = \pm 0.55$). The two dimensionality of the transition front and its movement with angle of attack indicates good tunnel flow quality and the absence of wall effects on the spanwise behavior of the front.
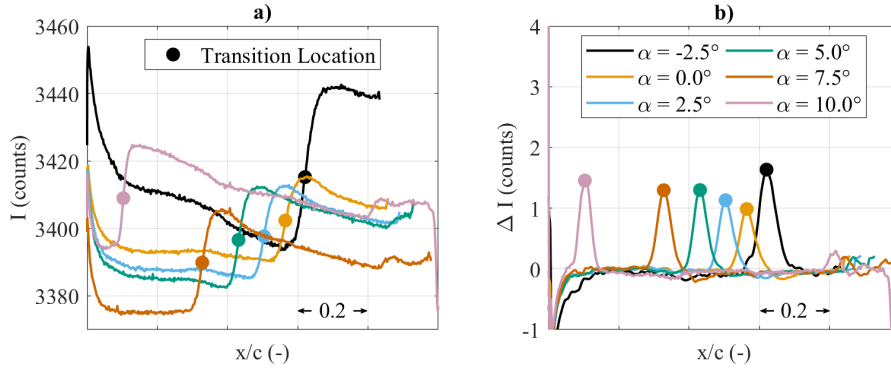

Figure 11. Left: Chord wise intensity profiles extracted from the data of Fig. 10 at $y/c = -0.4$. Right: First derivative of the intensity profiles shown on the left.

Figure 11a illustrates the intensity distributions for all measured angles of attack along the wing chord at a fixed spanwise position ($y/c = 0.4$) and corresponding to the orange lines shown in Fig. 10. The curves are at slightly different intensity levels due to differences in the overall temperature change of the wing model during different runs. Nevertheless, a noticeable increase in the measured intensity along the chord of approximately 20 counts is evident for all angles of attack considered. This increase denotes the location of BL transition. According to Weiss et al.[19], the position of 50 % turbulence intermittency is found at the highest gradient of the temperature in chordwise direction. The corresponding spatial gradient curves for the current test cases are reported in Fig. 11b, where a distinct maximum can be observed on each curve. The respective positions are marked as colored dots in both Fig. 11a and b. These results can be used as a benchmark for the interpretation of the transition under
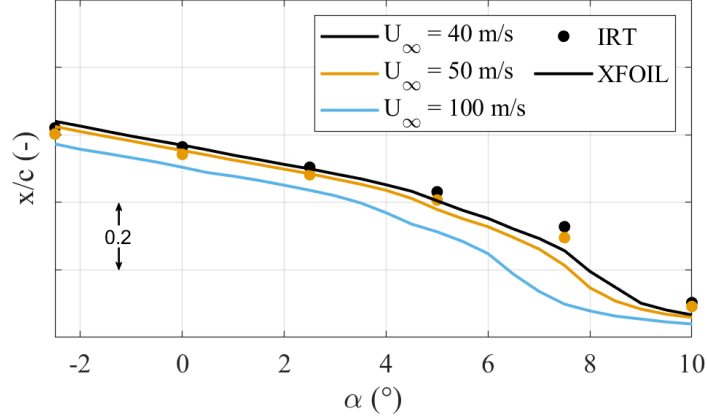
the influence of the propeller.

Figure 12. Transition locations as function of angle of attack for different inflow velocities measured with IRT and predicted with XFOIL.

The detected transition locations are plotted against the wing angle of attack for both wind tunnel freestream velocities ($U_\infty = 40\,\frac{m}{s}$ and $U_\infty = 50\,\frac{m}{s}$) in Fig. 12 as dots. The black dots are the same locations as depicted in Fig. 11. In addition to the IRT results, predicted transition locations from 2D XFOIL calculations with an $N_{\mathrm{crit}} = 9$ are shown as solid lines. The results confirm the expected trend of the BL transition location that moves towards the leading edge as the angle of attack increases. The effects of the wind tunnel freestream velocity (increased Reynolds number) are also consistent with the data collected. The previous 2D XFOIL analysis was also repeated at a freestream velocity of $U_\infty = 100\,\frac{m}{s}$, significantly higher than the maximum freestream velocity reached during the test ($U_\infty = 50\,\frac{m}{s}$). Such analysis was carried out to further assess the effects on the BL transition location of an increased inflow velocity due to the presence of the propeller in front of the wing model. As it will be shown later in this paper, the comparison between the measured BL transition location under the influence of the propeller and the 2D XFOIL results points to a possible combination of local induced inflow angle and propeller induced turbulence.

The intensity distributions in Fig. 13 are taken at an angle of attack $\alpha = -2.5°$ under the influence of the propeller. The image in Fig. 13a shows the previously discussed case without the propeller for comparison. The images in Fig. 13b-e result from different rotational speeds of the propeller. From Fig. 13b-d it can be seen that the propeller triggers an earlier onset of transition. Furthermore, the impact of the propeller blade tip vortices is clearly visible at $y/c = \pm\,0.7$ for 1000 rpm and 1200 rpm as transition cones starting at the leading-edge. The earlier onset of transition is a result of the increased turbulence in the propeller wake and the increased Reynolds number compared to the undisturbed wind tunnel flow. The propeller results in Fig. 13b-d show a rather symmetric transition region for positive and negative y/c. This points to a comparably low influence of the direction of rotation of the propeller (upwash/downwash). Furthermore, it can be seen that the transition line for the propeller cases is not as distinct as in the no propeller case.

To further investigate the transition topology under the influence of the propeller, intensity profiles similar to those in Fig. 11 at $\alpha = -2.5°$, but related to different rotational speeds are shown in Fig. 14 at a spanwise location at y/c=-0.4. From the resulting intensity levels it can
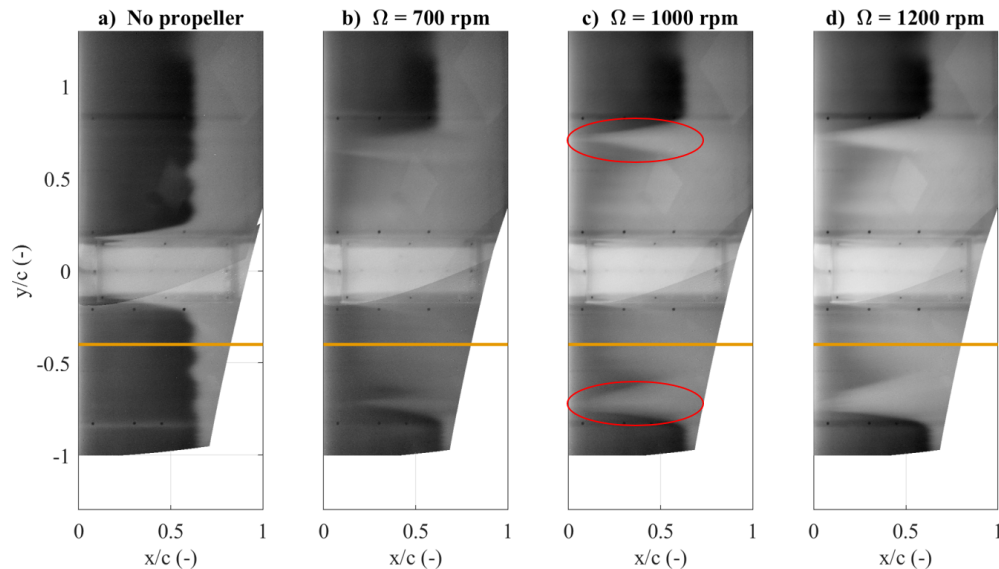
Figure 13. Average intensity distributions without the propeller (a) and with the propeller spinning at different rotational speeds (b-d), all at $\alpha = -2.5°$ and $U\infty = 40$ m/s. Footprints of the propeller blades' trailing vortices are highlighted in red.

be seen that the temperature increase in chordwise direction is not as distinct as in the case without the propeller. Therefore, the maxima of the gradients are less prominent and, thus, the measurement of the transition location is more ambiguous.

The process demonstrated in Fig. 14 can be repeated for every row in the y/c-direction to obtain the spanwise distribution of the transition location. Figure 15 shows the comparison of these spanwise distributions for different angles of attack (a-d) and propeller rotational speeds at a fixed wind tunnel freestream velocity of $U_\infty = 40 \frac{m}{s}$. The transition location distributions obtained with the propeller spinning are compared with the the unpowered case in each figure. The spanwise distribution of the transition location for the test cases shown in Fig. 13 at $\alpha = -2.5°$ are presented in Fig. 15a. Detected locations in the region of overlap with the boom ($|y/c| < 0.19$) were masked out. The comparison between the powered and unpowered cases clearly shows that the BL transition is not affected by the presence of the propeller in the portions of the wing that fall outside the propeller slipstream ($|y/c| > 0.85$, e.g. not directly hit by the propeller wake). A different behavior is observed in the wing portion that is affected by the propeller wake. As expected, in this region the BL tends to transition earlier than when the propeller is turned off. Due to the less prominent step in the chordwise intensity distribution (see Fig. 14) a scatter in the detected transition location occurs and the detected transition location is not as defined as outside of the propeller wake. As documented by Miley[20] and Howard[21], both flight test measurements and wind tunnel experiments carried out to investigate the effects of the propeller slipstream on a wing have shown that the BL cycles between a laminar and a turbulent state at the propeller blade passage rate. As the BL on a given point on the wing contour goes through distinct phases of turbulent, reverse-transitional, and laminar behaviour, the surface temperature of the wing model is also affected. This in turn leads to smoother temperature distributions as the images recorded by
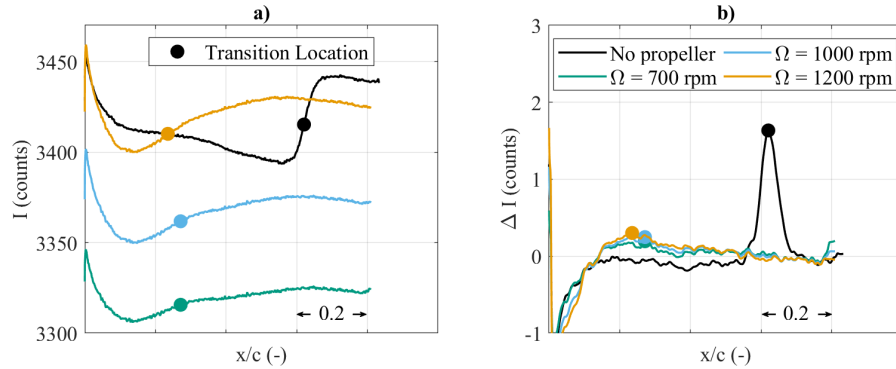
Figure 14. Left: Chord wise intensity profiles extracted from the data of Fig. 13 at $y/c = -0.4$. Right: First derivative of the intensity profiles shown on the left.

the IRT camera are temporally smoothed by the heat capacity of the wing surface and the integration time of the camera exposure. Different phenomena may cause the earlier onset in the portion of the wing blown by the propeller wake. Both an increased inflow velocity and turbulence level in the propeller wake may lead to an earlier onset of the BL transition on the wing compared to the unpowered cases. Based on the 2D XFOIL calculations at $U_\infty = 100 \frac{m}{s}$ the influence of an increased inflow velocity (and thus increased Reynolds number) alone can be estimated. The XFOIL calculated transition position occurs at higher x/c (further downstream) than documented in the IRT measurement in the region of the propeller wake. This implies that the earlier transition onset in the region of the propeller wake cannot be ascribed to the increased inflow velocity alone. At the slipstream boundaries ($|y/c| \approx 0.7$) the aforementioned cones triggered by the propeller blade tip vortices are observed.

4.0 CONCLUSIONS

An experimental wind tunnel test campaign aimed at characterizing the aerodynamic interaction between a wing section and propellers mounted on a boom was presented. In particular the cruise flight condition was investigated by means of pressure measurements on the wing surface and an infrared thermography technique in order to assess the laminar-to-turbulent transition of the BL on the wing upper surface, with and without the forward propeller.

Pressure distributions measured by means of pressure taps placed above and below the boom location and grouped in belts on four wing sections were presented. Results show the interactional effect of the blowing propeller on the local wing performance that provide an opposite increase/decrease of sectional lift with respect to propeller rotation axis due to the upwash/downwash provided by the blades.

Concerning infrared thermography technique, the averaged temperature maps for the wing without the tilter propeller were considered as reference. For the no tilter propeller case, the transition line is clearly visible and moves forward as the angle of attack changes in the range $-2.5°$ to $10°$. As expected, even though the gradients are captured with few counts, a sharp line denoting the transition location advancing from the trailing–edge toward the leading–edge as the angle of attack increases was found. The steep derivative of the temperature gradient extracted from the chordwise intensity profiles allows precise identification of the position of the laminar–turbulent transition. Minor disturbances in the shape of the transition line are due
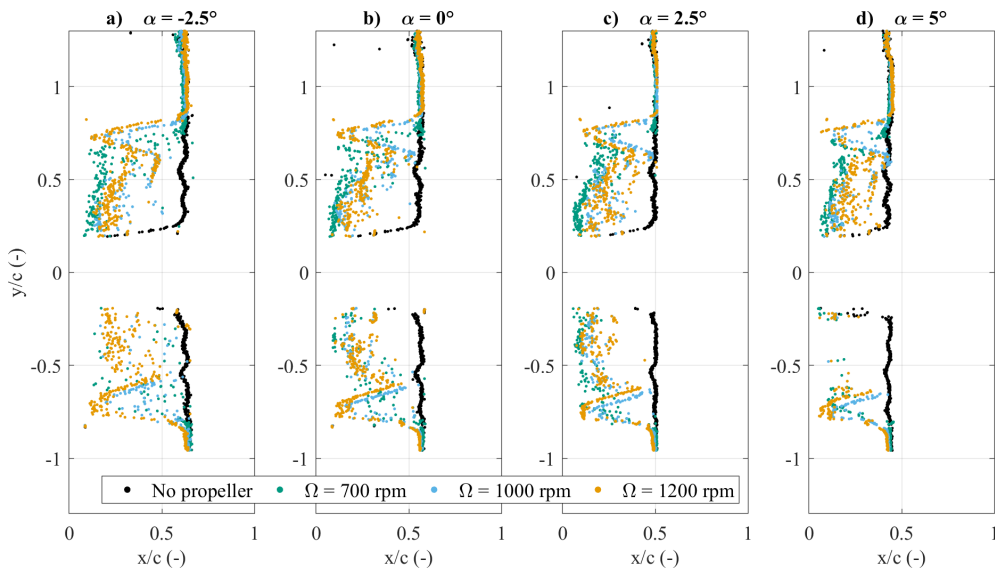
Figure 15. Spanwise distribution of detected transition locations with propeller spinning and turned off at different angles of attack and rotational frequencies at a wind tunnel freestream velocity of $U_\infty = 40\,\text{m/s}$.

to the presence of surface static pressure taps. Moreover the transition region proves to be symmetric above and below the boom (see Figure.10), while no valuable information can be inferred from the temperature maps where the boom is located.

With the addition of the propeller spinning interesting results were obtained, as it can be noticed how the transition onset moves forward with respect to the case without the propeller (reference case $\alpha=-2.5°$). Moreover, the impact of the tip vortices of the blades are visible as transition cones starting from the leading-edge. The propeller triggers an earlier transition due to the increase in turbulence and the local Reynolds number in the blade wake if compared with the undisturbed wind tunnel flow. It's also interesting to note that the transition region remains symmetric on the upwash/downwash sides of the blade, indicating little influence of the blade rotational direction. The chordwise intensity levels for the case with rotation show less pronounced gradients than the reference no rotation case.

Generally speaking, the wind tunnel test campaign provided a comprehensive experimental data set, allowing all goals for the campaign to be met. The use of full-scale components of a flying eVTOL aircraft helped to provide a thorough validation of the aircraft performance as computed by CFD solvers with different levels of fidelity. The campaign results represent an interesting database for the evaluation of interactional effects between propeller and wing for eVTOL aircraft.

ACKNOWLEDGEMENTS

Declaration of Interests

The authors declare that they have no known competing financial interests or personal relationships that could have appeared to influence the work reported in this paper.

REFERENCES

1. Polaczyk, N., Trombino, E., Wei, P., and Mitici, M., "A Review of Current Technology and Research in Urban On-Demand Air Mobility Applications," Proceedings of the Vertical Flight Society's 6th Annual Electric VTOL Symposium, 29–31 January 2019.

2. Johnson, W., Silva, C., and Solis, E., "Concept Vehicles for VTOL Air Taxi Operations," Proceedings of the AHS Technical Conference on Aeromechanics Design for Transformative Vertical Flight, January 16-19 2018.

3. Silva, C., Johnson, W., Solis, E., Patterson, M. D., and Antcliff, K. R., "VTOL Urban Air Mobility Concept Vehicles for Technology Development," Proceedings of the AIAA Aviation Technology, Integration, and Operations Conference, June 25-29 2018.

4. Zanotti, A., and Algarotti, D., "Aerodynamic interaction between tandem overlapping propellers in eVTOL airplane mode flight condition," *Aerospace Science and Technology*, Vol. 124, 2022, pp. 107518. DOI: https://doi.org/10.1016/j.ast.2022.107518

5. Hooker, J. R., Wick, A., Ginn, S. R., Walker, J., and Schiltgen, B. T., "Overview of low speed wind tunnel testing conducted on a wingtip mounted propeller for the workshop for integrated propeller prediction," AIAA AVIATION 2020 FORUM, 2020.

6. Sinnige, T., van Arnhem, N., Stokkermans, T. C. A., Eitelberg, G., and Veldhuis, L. L. M., "Wingtip-Mounted Propellers: Aerodynamic Analysis of Interaction Effects and Comparison with Conventional Layout," *Journal of Aircraft*, Vol. 56, (1), 2019, pp. 295–312. DOI: 10.2514/1.C034978

7. Alvarez, E., Mehr, J., and Ning, A., "FLOWUnsteady: An Interactional Aerodynamics Solver for Multirotor Aircraft and Wind Energy," AIAA AVIATION 2020 FORUM, 2020.

8. Zhou, B., Morelli, M., Gauger, N. R., and Guardone, A., "Simulation and Sensitivity Analysis of a Wing-Tip Mounted Propeller Configuration from the Workshop for Integrated Propeller Prediction (WIPP)," AIAA AVIATION 2020 FORUM, 2020.

9. Stokkermans, T. C. A., van Arnhem, N., Sinnige, T., and Veldhuis, L. L. M., "Validation and Comparison of RANS Propeller Modeling Methods for Tip-Mounted Applications," *AIAA Journal*, Vol. 57, (2), 2019, pp. 566–580. DOI: 10.2514/1.J057398

10. Van Arnhem, N., *Unconventional Propeller-Airframe integration for transport aircraft configurations*, Ph.D. thesis, Delft University of Technology, 2022.

11. Wolf, C. C., Gardner, A. D., and Raffel, M., "Infrared thermography for boundary layer transition measurements," *Meas. Sci. Technol.*, Vol. 31, 2020, pp. 1–21.

12. Zanotti, A., Rausa, A., Grassi, D., Riccobene, L., Gibertini, G., Guardone, A., Auteri, F., Braukmann, J., and Schwarz, C., "Infrared Thermography Measurements over a Tail-Plane Model of a Large Passenger Aircraft," *Journal of Physics: Conference Series*, Vol. 2293, (1), 2022, pp. 012014.

13. Gardner, A. D., Wolf, C. C., Heineck, J. T., Barnett, M., and Raffel, M., "Helicopter

rotor boundary layer transition measurement in forward flight using an infrared camera," *Journal of the American Helicopter Society*, Vol. 65, (1), 2020, pp. 2–14(13).

14. Gibertini, G., Gasparini, L., and Zasso, A., "Aerodynamic design of a civil-aeronautical low speed large wind tunnel," Proceedings of the AGARD 79th fluid dynamics panel symposium, May 1996.

15. Derlaga, C. W., M.D. Jackson, and Buning, P. G., "Recent Progress in OVERFLOW Convergence Improvements," AIAA SciTech Forum, January 2020.

16. Hildebrand, N., Chang, C.-L., Choudhari, M., li, F., and nielsen, E., "Coupling of the FUN3D Unstructured Flow Solver and the LASTRAC Stability Code to Model Transition," AIAA SciTech Forum, January 2022.

17. Tugnoli, M., Montagnani, D., Syal, M., Droandi, G., and Zanotti, A., "Mid-fidelity approach to aerodynamic simulations of unconventional VTOL aircraft configurations," *Aerospace Science and Technology*, Vol. 115, 2021, pp. 106804.

18. Klein, C., Engler, R. H., Henne, U., and Sachs, W. E., "Application of pressure-sensitive paint for determination of the pressure field and calculation of the forces and moments of models in a wind tunnel," *Experiments in Fluids*, Vol. 39, (2), July 2005, pp. 475–483. DOI: 10.1007/s00348-005-1010-8

19. Weiss, A., Gardner, A. D., Klein, C., and Raffel, M., "Boundary-layer transition measurements on Mach-scaled helicopter rotor blades in climb," *CEAS Aeronautical Journal*, Vol. 8, (4), September 2017, pp. 613–623. DOI: 10.1007/s13272-017-0263-2

20. Miley, S., Howard, R., and Holmes, B., "Wing laminar boundary layer in the presentce of a propeller slipstream," *Journal of Aircraft*, Vol. 25, (7), 1988, pp. 606–611. DOI: 10.2514/3.45630

21. Howard, R., *An investigation of the effects of the propeller slipstream on a wing boundary layer*, Ph.D. thesis, Texas A&M University, College Station, dec 1987.